Title

Stochastic dynamics of intermittent pore-scale particle motion in three-dimensional porous media: Experiments and theory

Journal

Geophysical Research Letters, 44(18)

ISSN

0094-8276

Authors

Morales, VL
Dentz, M
Willmann, M
et al.

Publication Date

2017-09-28

DOI

10.1002/2017gl074326

Peer reviewed

AGU PUBLICATIONS

Geophysical Research Letters

RESEARCH LETTER
10.1002/2017GL074326

Key Points:
- Pore-scale particle transport in porous media is experimentally studied
- Lagrangian velocities are well correlated, lognormally distributed, and nonstationary
- Time evolution of the velocity process is explained by a Markov chain with multiplicative noise

Supporting Information:
- Supporting Information S1
- Data Set S1
- Data Set S2
- Data Set S3

Correspondence to:
V. L. Morales,
vermorales@ucdavis.edu

Citation:
Morales, V. L., M. Dentz, M. Willmann, and M. Holzner (2017), Stochastic dynamics of intermittent pore-scale particle motion in three-dimensional porous media: Experiments and theory, *Geophys. Res. Lett.*, *44*, doi:10.1002/2017GL074326.

Received 9 JUN 2017
Accepted 13 AUG 2017
Accepted article online 17 AUG 2017

Stochastic dynamics of intermittent pore-scale particle motion in three-dimensional porous media: Experiments and theory

V. L. Morales[1,2], M. Dentz[3], M. Willmann[2], and M. Holzner[2]

[1]Department Civil and Environmental Engineering, Ghausi Hall, University of California, Davis, California, USA, [2]Institute of Environmental Engineering, ETH Zürich, Zürich, Switzerland, [3]Spanish National Research Council (IDAEA-CSIC), Barcelona, Spain

Abstract We study the evolution of velocity in time, which fundamentally controls the way dissolved substances are transported and spread in porous media. Experiments are conducted that use tracer particles to track the motion of substances in water, as it flows through transparent, 3-D synthetic sandstones. Particle velocities along streamlines are found to be intermittent and strongly correlated, while their probability density functions are lognormal and nonstationary. We demonstrate that these particle velocity characteristics can be explained and modeled as a continuous time random walk that is both Markovian and mean reverting toward the stationary state. Our model accurately captures the fine-scale velocity fluctuations observed in each tested sandstone, as well as their respective dispersion regime progression from initially ballistic, to superdiffusive, and finally Fickian. Model parameterization is based on the correlation length and mean and standard deviation of the velocity distribution, thus linking pore-scale attributes with macroscale transport behavior for both short and long time scales.

Plain Language Summary Transport of dissolved substances in rocks and soils are controlled by the intricacies of the pore space. In short time scales, brief bursts of fast flow in otherwise slow-moving water lead to intense spreading. In long time scales and/or distances, this burst effect is drowned out and spreading behavior becomes weak and constant. The long time behavior is well understood and predictable, but not the short time behavior and their transition. We study the processes responsible for this transition from intense to weak spreading behavior. In the laboratory, we track how small particles in water move through the pore spaces of a transparent, synthetic soil. These measurements show us how long the fast flow bursts last, how fast they are, and how frequently they occur. Statistical analysis of the particle behavior reveals that flow has a short term memory, and we build a predictive model that captures this effect. Our novel model allows predictions of the changeover from intense to weak spreading, and demonstrates that it captures fundamental transport processes in naturally-occurring porous media. Therefore, this new model can be used to make better predictions for important applications such as groundwater contamination assessments or oil recovery.

1. Introduction

Understanding how flow and transport through porous media are regulated by structural features of the pore space is a problem of central concern for many environmental matters not limited to the following: reactive transport in groundwater [*Neuman*, 1990; *Willmann et al.*, 2010; *Dentz et al.*, 2011], environmental remediation [*Freedman and Gossett*, 1989; *Zhang*, 2003], nuclear waste disposal [*McCarthy et al.*, 1978; *Helton*, 1993], and oil recovery [*Hiorth et al.*, 2010; *Armstrong and Wildenschild*, 2012]. Predicting flow behavior in heterogeneous porous media from measurable structural properties remains a challenge, given that the relationship between structure and function is tenuously understood. Transport even in homogeneous porous media tends to display tailing in breakthrough curves, nonlinear evolution of mean square displacement, and non-Gaussian spatial density profiles, which are signature features of anomalous (non-Fickian) behavior. As a result, advection-dispersion formulations are unsuitable for capturing preasymptotic transport [*Lester et al.*, 2014]. Modeling approaches typically assume diffusion in porous media to be Gaussian at the Darcy scale [*Koch and Brady*, 1985] and attribute anomalous features to larger-scale heterogeneities. However, recent studies have drawn attention to the interplay between persistent pore-scale velocity heterogeneity

and anomalous transport [*Bijeljic et al.*, 2004; *Datta et al.*, 2013; *de Anna et al.*, 2013; *Clotet et al.*, 2014; *de Anna et al.*, 2014; *Kang et al.*, 2014; *Siena et al.*, 2014; *Holzner et al.*, 2015], thus highlighting the mutiscale complexity of transport processes in porous media.

It is well accepted that large-scale processes are fundamentally controlled by the collective interactions between the fluid and the pore space structure. A major challenge for modeling pore-scale transport is to determine how much detail of the pore geometry is needed to make accurate predictions of macroscopic processes. Various pore-scale upscaling models have been proposed to extract the relevant mechanisms that control transport in porous media, albeit with a trade-off between computational efficiency and faithful representation of the real pore geometry. Take, for instance, the geometric simplification of the pore space through use of sinusoidal wavy channels in theoretical studies of pore-scale reactive transport [*Bolster et al.*, 2009; *Le Borgne et al.*, 2011; *Sund et al.*, 2015]. Such idealized pore approaches approximate the transit time distribution and spatial correlation properties of more complex media, which permits modeling sizable samples with ease. Network models are a step-up in realism but still reduce the pore system to a multidimensional lattice of edges and nodes that must be tuned to match the pore size correlation and topological disorder of the real system they represent [*Fatt*, 1956; *Blunt*, 2001; *Dong and Blunt*, 2009]. Direct numerical models on pore-scale images honor the geometry of the pore space to the limit of the image resolution but are highly computationally demanding and avert simulations on large samples [*Blunt et al.*, 2013; *Bijeljic et al.*, 2013].

The continuous time random walk (CTRW) model has become a growingly popular framework for predicting anomalous transport in heterogeneous media [*Dentz and Berkowitz*, 2003; *Berkowitz et al.*, 2006; *de Anna et al.*, 2013; *Kang et al.*, 2014; *Le Borgne et al.*, 2011; *Holzner et al.*, 2015; *Le Borgne et al.*, 2008; *Sund et al.*, 2015; *Tyukhova et al.*, 2016]. At its core, CTRW models describe effective transport by discretizing the solute into a large number of particles that move as a sequence of transitions in space and time. Space increments are typically fixed to match the characteristic length of the porous medium, while time increments are randomly sampled from a given transition time distribution. The basic model assumes that time increments between successive jumps are independent and identically distributed. Yet numerous studies have conclusively demonstrated that correlation between successive steps is required to correctly reproduce certain transport features [*Kang et al.*, 2014, 2015; *de Anna et al.*, 2013; *Le Borgne et al.*, 2008; *Meyer and Bijeljic*, 2016]. Several approaches have been proposed to enforce correlation in the Lagrangian velocity along a particle trajectory. *Holzner et al.* [2015] implement correlation through a persistence of particle velocity parameter that allows a particle to change velocities at turning points based on a probabilistic value. The work by *Le Borgne et al.* [2008] and the various others that follow it [*Kang et al.*, 2014, 2015; *Le Borgne et al.*, 2011; *Sund et al.*, 2015; *de Anna et al.*, 2013] effects a conditional correlation via velocity transition matrices, which condition the probability density of transition time on the observed value in the previous step. *Meyer and Bijeljic* [2016] more recently account for velocity correlations through a velocity-direction-angle process that reflects the recurrent focusing and defocusing of flow at the pore scale. While the above Markovian approaches reproduce some aspects of transport behavior relatively well, the former two do not accurately simulate subpore velocity fluctuations and the latter requires a great detail of particle dynamics as input.

In this work, we study the stochastic dynamics of Lagrangian velocity in porous media with particular emphasis on the velocity evolution process. First, transport is studied experimentally by tracking tracer particles along streamlines in three different porous structures. Then, a new simple predictive model that follows an Ornstein-Uhlenbeck process is proposed to recover the progression of Lagrangian velocities. In section 2 we present the experimental procedure and statistical methods for empirical data analysis. In section 3 we analyze and interpret the experimental data in terms of particle displacement, as well as velocity correlation, distributions, and increments. In section 4 we introduce the new model and introduce the values needed for its parameterization. Lastly, we demonstrate the model capabilities to faithfully reproduce the pore-scale statistics and general transport behavior and discuss its sensitivity to input parameter uncertainty.

2. Methods

In the following, we outline the methods for experimentation and analysis of the particle position and velocity data.

2.1. Experimental Materials and Methods

A transparent porous medium is created by matching the refractive index of the working solution with that of the granular material. Nafion grains are used as the porous medium, and the working solution is a mixture

of isopropanol with deionized water (42 vol/vol %). A cubic flow-through cell ($L = 3.8 \times 10^{-2}$ m per side with 4 mm diameter inlet/outlet connections at the center of the top/bottom sides) is wet packed with the granules and the pore space maintained fully saturated with solution throughout the experiment duration. Mixtures of two classes of Nafion grains of diameter $d_1 = 3.6$ mm and $d_2 = 0.5$ mm are used to create three different realizations of heterogeneous structures, labeled *A*, *B*, and *C*. Respectively, the mean grain diameter (d_{50}) and characteristic pore size are 3.60×10^{-3} and 1.07×10^{-3} for sample *A*, 2.57×10^{-3} and 5.46×10^{-4} for sample *B*, and 2.05×10^{-3} and 2.92×10^{-4} for sample *C*. Imposed volumetric flow rates, *Q*, in the range of $1.25 \times 10^{-7} - 2.50 \times 10^{-7}$ m^3/s give Reynolds numbers ($Re = v_{av} d_{50}/\nu < 1$), ruling out the occurrence of recirculation zones. The average flow speed is calculated as $v_{av} = Q/(L^2\epsilon)$, where $\epsilon \sim 0.35$ is porosity. d_{50} is the mean grain size and $\nu = 1.84 \times 10^{-6}$ m^2/s is the kinematic viscosity of the isopropanol solution. Neutrally buoyant fluorescent particles of 1 g/cm^3 density and 68 μm diameter (volume fraction concentration ~0.01%) are used to seed the solution with flow tracers. Manufacturer details of the materials are provided in the supporting information.

To trace flow particles in the transparent porous medium, a three-dimensional particle tracking velocimetry (3D-PTV) technique is used to record the position of approximately 400 individual particles in *x*, *y*, and *z* coordinates per frame. The setup consists of a 20 W Ar-Ion laser as the light source for exciting the fluorescent particles, a Photron high speed camera with a resolution of 1024 × 1024 pixels operated at a frame rate of 50 Hz, and a four-way image splitter for stereoscopic viewing of the sample. For additional details of 3D-PTV the reader is referred to *Holzner et al.* [2015] and *Hoyer et al.* [2005]. The setup used here permits particle positions to be determined with an accuracy of ~ 10 μm (see Figure S1 for a 3-D view of the trajectories). The average recording period per experiment is 4 min, during which new particles constantly enter the interrogation volume at the inlet and exit through the outlet. Individual particle tracks tend to be fragmented due to temporary loss of view in pores with high particle density. To address this, postprocessing as per the method proposed by *Xu* [2008] is used to rejoin interrupted trajectories, reduce the particle position noise, and increase the quality of Lagrangian velocities along trajectories. Strict maximum gap tolerances in space (180 μm) and time (0.04 s) are set for joining candidate trajectories, which were verified to have no influence on the outcomes or intermittentcy (see supporting information, section S3 for more details). Lastly, postprocessed particles tracked for less than 0.01 s are discarded, leaving each experiment with $\mathcal{O}(10^4)$ trajectories to work with, spanning a maximum length of ~10 pores.

2.2. Data Analysis

Particle velocities are analyzed both isochronally and equidistantly along trajectories. To define these particle velocities, we first consider the evolution of the particle position $\mathbf{x}(t;\mathbf{a})$, which is given by the advection equation

$$\frac{\mathrm{d}\mathbf{x}(t;\mathbf{a})}{\mathrm{d}t} = \mathbf{v}(t;\mathbf{a}). \tag{1}$$

The initial position is $\mathbf{x}(t=0;\mathbf{a}) = \mathbf{a}$. The particle velocity $\mathbf{v}(t;\mathbf{a})$ is related to the flow velocity $\mathbf{u}(\mathbf{x})$ as $\mathbf{v}(t;\mathbf{a}) = \mathbf{u}[\mathbf{x}(t;\mathbf{a})]$. The coordinate vector is $\mathbf{x} = (x, y, z)^\top$; the velocity vectors are $\mathbf{v} = (v_x, v_y, v_z)^\top$ and $\mathbf{u} = (u_x, u_y, u_z)^\top$. The distance $s(t;\mathbf{a})$ traveled along a streamline is given by

$$\frac{\mathrm{d}s(t;\mathbf{a})}{\mathrm{d}t} = v_t(t;\mathbf{a}) \tag{2}$$

with $v_t(t;\mathbf{a}) = |\mathbf{v}(t;\mathbf{a})|$. The travel time along a trajectory is given by

$$\frac{\mathrm{d}t(s;\mathbf{a})}{\mathrm{d}s} = \frac{1}{v_s(s;\mathbf{a})} \tag{3}$$

with $v_s(s;\mathbf{a}) = v_t[t(s;\mathbf{a});\mathbf{a}]$, see also *Dentz et al.* [2016]. The data consist of an ensemble of position time series $\{\mathbf{x}(t;\mathbf{a})\}$. In the following, the initial position $\mathbf{a}$ in the arguments of particle positions, displacements, and velocities is omitted for compactness of notation. The average over the ensemble of particles is denoted by angular brackets $\langle\cdot\rangle$. Velocity is sampled isochronally from the data according to equation (2) and equidistantly according to equation (3). In the following section, we provide a statistical analysis of the particle displacement $s(t)$ and velocity data, referring to $v_t(t)$ as t-Lagrangian velocity and $v_s(s)$ as s-Lagrangian velocity.

3. Statistical Analysis of Displacement and Velocity Data

In this section, we analyze the displacement and velocity data to identify and quantify the stochastic dynamics of particle motion. To this end, we first consider the first and second centered displacement moments and their temporal evolution. Then, we quantify the correlation of particle velocities along trajectories. Finally, we analyze the distribution of particle velocities and velocity increments and their evolution in time. The information obtained in this section provides the basis for the stochastic model of particle motion derived in the next section.

3.1. Displacement Statistics

We consider here particle displacement $s(t)$ along streamlines. The data are analyzed in terms of the mean $m(t)$ and centered mean square $\sigma^2(t)$ displacements. These quantities provide information on the statistical moments of the pore-scale velocity distribution.

Early and late times are here defined with respect to the characteristic advection time scale, which is given by

$$\tau_v = \frac{\lambda_v}{v_c}. \tag{4}$$

Here the average over all velocity data is v_c, and the characteristic length λ_v is of the order of the size of a pore throat and defined below in terms of the velocity correlation along trajectories. The displacement data cover a time range of about $10\tau_v$.

3.1.1. Mean Displacement

Particles are released in a small volume at the center of the inlet boundary. Thus, particles cannot in general sample the full velocity variability and, as a result, the velocity statistics are not stationary. This is observed for the mean displacements in all three medium samples, as illustrated in Figures 1a–1c. It is evident that the average particle velocity

$$v_a(t) = \frac{\mathrm{d}m(t)}{\mathrm{d}t} \tag{5}$$

is variable for all samples.

The largest velocity is observed at early times $t \ll \tau_v$ (denoted by the subscript "0"), for which $v_a(t) = \langle v_0 \rangle$. We find average short time velocity values of $\langle v_0 \rangle = 1.5 \times 10^{-3}$, 2.4×10^{-3}, and 1.1×10^{-3} m/s for samples *A*, *B*, and *C*, respectively. For late times $t > \tau_v$ (denoted by the subscript "ℓ"), the average particle velocities then relax toward a constant late time value $\langle v_\ell \rangle$, which we identify to be equivalent to the Eulerian mean velocity. We find these values to be $\langle v_\ell \rangle = 1.0 \times 10^{-3}$, 1.7×10^{-3}, and 9.3×10^{-4} m/s for samples *A*, *B*, and *C*, respectively.

3.1.2. Displacement Variance

The displacement variance $\sigma^2(t)$ characterizes the spreading of the particle plume. Its evolution for the different samples is shown in Figures 1d–1f. It exhibits two distinct displacement regimes. At early times $t \ll \tau_v$ the behavior is ballistic. We obtain for the variance of the initial velocities the values $\sigma^2_{v_0} = 2.0 \times 10^{-6}$, 6.2×10^{-6}, and 9.6×10^{-7} m^2/s^2 for samples *A*, *B*, and *C*, respectively.

At $t \approx \tau_v/3$ the behavior crosses over from ballistic to a superlinear evolution. From the recording window of $\sim 10\tau_v$, it is not possible to identify a crossover to diffusive regimes for long times, i.e., linear Fickian regime is not reached during the recording time of any experimental run. We clearly observe that $\sigma^2(t)$ evolves faster than linear. It is worth noting that the range of superlinear behavior observed is in good agreement with observations from direct numerical simulations in images from Berea and Bentheimer sandstone samples [*Kang et al.*, 2014; *Meyer and Bijeljic*, 2016]. Differences in the evolution of $\sigma^2(t)$ between the three samples for $t > \tau_v$ reflect the respective flow field heterogeneity. The displacement variances for the relatively homogeneous samples *A* and *B* evolve as $\sim t^{1.3}$, while the more heterogeneous sample C evolves faster as $\sim t^{1.5}$. While the above noted particle dynamics results from interactions with the structural heterogeneity of the medium, their elucidation remains the subject of ongoing work.

3.2. Velocity Autocorrelation

We consider here the correlation properties of subsequent particle velocities. Figure 2 illustrates representative velocity time series recorded along single trajectories for each sample. We observe intermittent behavior that is characterized by long correlated periods of low-velocity interrupted by short bursts of high velocity. This can be explained by the existence of a characteristic velocity correlation length scale λ_v [*Dentz et al.*, 2016].

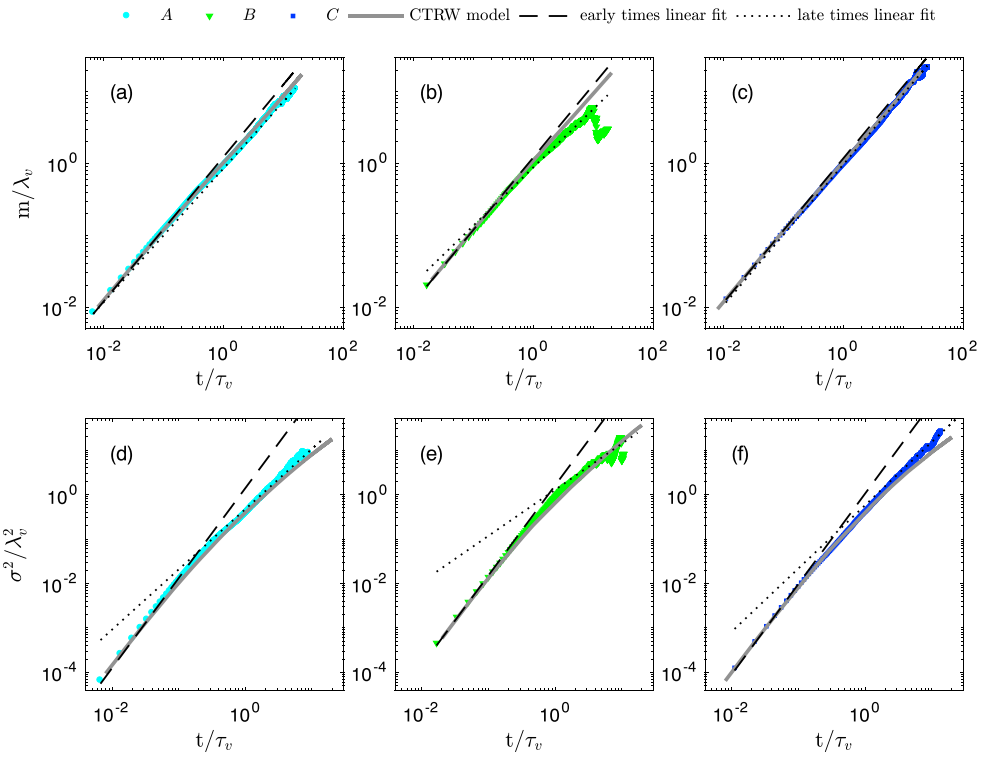

Figure 1. Symbols are (a–c) normalized mean displacement or (d–f) mean square displacement of tracer particles over normalized time for samples *A* (Figures 1a and 1d), *B* (Figures 1b and 1e), and *C* (Figures 1c and 1f). Dashed and dotted lines are the linear fits for the early and late times, respectively. Solid lines are predictions of the CTRW model.

The persistence time is given by λ_v/v_s where v_s is the s-Lagrangian velocity. The duration of high-velocity episodes is thus much smaller than for low velocities.

λ_v is estimated from the integral of the covariance function of s-Lagrangian velocities (refer to supporting information, for quantitative details), giving $\lambda_v = 1.4 \times 10^{-3}$, 2.4×10^{-3}, and 7.0×10^{-4} m for samples *A*, *B*, and *C*, respectively. These values correspond well to the characteristic pore lengths of each sample, which are $\ell_p = 1.0 \times 10^{-3}$, 5.5×10^{-4}, and 2.9×10^{-4} m for samples *A*, *B*, and *C*, respectively. Thus, the velocity correlation scale is $\sim 1-4$ times the characteristic pore length. The existence of a constant correlation distance for the s-Lagrangian velocities suggests that the velocity series follows a Markov process [*Dentz et al.*, 2016].

3.3. Distributions of Lagrangian Velocities

To understand the particle dynamics, we quantify the distribution of particle velocities, which, together with the correlation length, gives information on particle residence and transition times in the porous medium. Thus, in this section, we study the distributions of t-Lagrangian particle velocities $v_t(t)$ to gain insight into the evolution of velocity distribution. The global t-Lagrangian velocity probability density function (PDF) $\mathcal{P}(v)$ is obtained by sampling of all velocity data as

$$\mathcal{P}(v) = \frac{1}{N_p} \sum_{i=1}^{N_p} \frac{1}{T_i} \int_0^{T_i} \mathrm{d}t \frac{\mathbb{I}[v \le v_t(t; \mathbf{a}_i) < v + \Delta v]}{\Delta v}, \tag{6}$$

where Δv is the sampling interval, N_p the number of sampled trajectories, and T_i the duration of trajectory *i*. As pointed out above, the velocity statistics here are nonstationary due to the nonstationary initial velocity distribution. Thus, $\mathcal{P}(v)$ can be seen as a mixture of the velocity PDFs at early and late times.

As discussed in *Dentz et al.* [2016] under ergodic conditions, particles can sample the full velocity spectrum along streamlines. In doing so, the velocity PDF evolves from its initial velocity distribution toward the steady

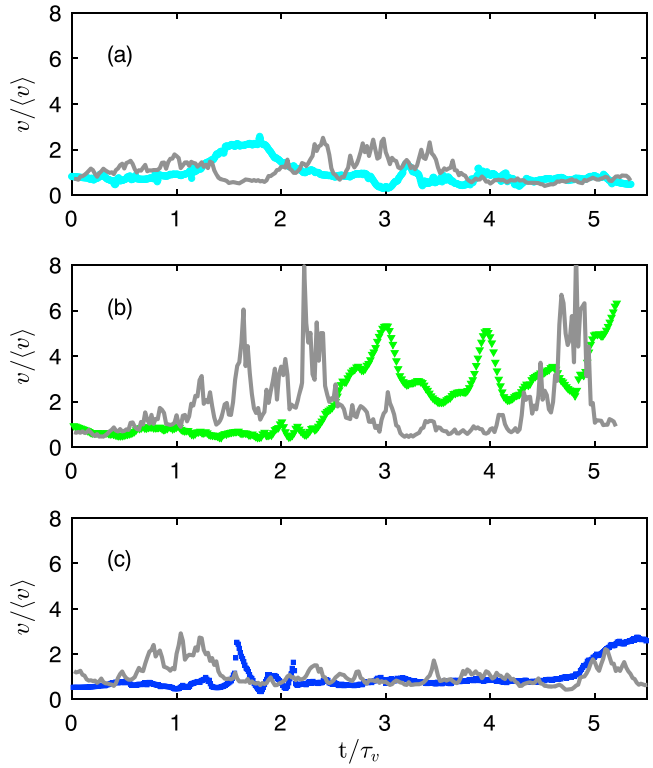

Figure 2. Symbols are time series of exemplary t-Lagrangian particle velocities for structures (a) *A*, (b) *B*, and (c) *C*. Gray lines correspond to simulated isochrone trajectories from the CTRW model.

state distribution. The steady state distribution then is equal to the Eulerian velocity distribution because of volume conservation. At times smaller than the advection time scale τ_v, the particle velocities reflect the initial velocity statistics. This is indicated by the mean displacements in Figures 1a–1c, which display a constant slope for $t < \tau_v$. Details about the early and late time velocity sampling are in the supporting information.

The bulk of the distribution as well as the decay at high velocities can be approximated by the lognormal distribution

$$p_i(v) = \frac{\exp\left\{-\frac{[\ln(v)-M_i]^2}{2\Sigma_i^2}\right\}}{v\sqrt{2\pi\Sigma_i^2}}, \tag{7}$$

where $i = 0, \ell$. Mean M_i and variance Σ_i^2 are related to the mean and variance of the early v_0 and late time v_ℓ velocities as

$$M_i = \ln\left(\frac{\langle v_i\rangle^2}{\sqrt{\sigma_i^2 + \langle v_i\rangle^2}}\right) \qquad \Sigma_i = \sqrt{\ln\left(\frac{\sigma_i^2 + \langle v_i\rangle^2}{\langle v_i\rangle^2}\right)}. \tag{8}$$

Figure 3 shows the velocity distribution at early ($t = 0$), late times ($t \geq \tau_v$), and global (i.e., all measured times) for sample *A*. Equivalent plots for samples *B* and *C* are found in the supporting information. Parameters referring to these early and late time instances are labeled by the subscripts 0 and ℓ, respectively. Noteworthy observations of the different velocity distributions include the higher probability for faster velocities at early times, and the similarity between the late time and global distributions. Like the global PDF, early and late time velocity PDFs can be well approximated by a lognormal distribution. Of particular importance is the velocity distribution at early times, which controls preasymptotic particle motion, and is due to the experimental injection conditions. The similarity of the global and late time velocity PDFs indicates that the sample of all trajectories may be considered stationary. For the prediction of preasymptotic particle transport, however, it is important to characterize the initial velocity distribution as observed in section 3.1.

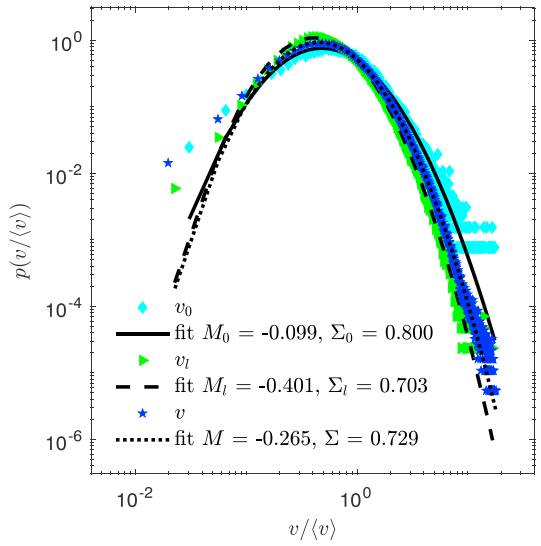

Figure 3. Probability density functions of t-Lagrangian velocities of structure *A* corresponding to early time ($t = 0$, diamonds), late time ($t \geq \tau_v$, arrows), and all times (pentagons). Lines indicate the lognormal fit to each distribution with their corresponding *M* and Σ parameters.

3.4. PDF of Velocity Increments

To study and characterize the fluctuations in particle velocities along streamlines, and specifically their intermittent character, we examine the statistical properties of t-Lagrangian velocity increments for various time delays τ,

$$\Delta_\tau v_t(t) = v_t(t+\tau) - v_t(t), \qquad (9)$$

where τ is the lag time between particle velocities. The behavior of $\Delta_\tau v_t(t)$ gives insight into the stochastic nature of particle transport [*de Anna et al.*, 2013]. For example, classical Langevin models for particle velocities assume that $v_t(t)$ follows an Ornstein-Uhlenbeck process [*Pope*, 2000], which predict that the velocity increment obeys Gaussian statistics for time increments larger than a characteristic correlation time. Deviations from such a behavior indicate intermittent properties, which may be due to strong correlation of particle velocities or strong tails in the velocity distributions. The velocity time series illustrated in Figure 2 indicate intermittent behaviors because of the strong temporal correlation in low-velocity periods and rapid fluctuations at high velocities.

In the following, we study how these behaviors manifest in the PDF of the velocity increments defined in (9), as normalized by its variance $\sigma^2_\Delta(\tau) = \langle \Delta_\tau v_t^2 \rangle$. To this end, we sample velocity increments over all particle trajectories and times. Figure 4 shows the measured distributions of normalized velocity increments for the three structures investigated. The shortest time lag captures the acceleration distribution. At short time lags the distributions are similar and symmetric, with exponential tails that reflect large-velocity jumps and a sharp peak at $\Delta v/\sigma_{\Delta v} = 0$ that indicates trapping in stagnant low-velocity zones. At longer lags the distributions progressively evolve toward an exponential shape but remain far from Gaussian. Structure *B* sustains heavier exponential tails and sharper peaks at longer time lags than structures *A* and *C*. This corroborates the intermittency and intensity variability across the different samples already observed in analyses prior. Intermittency is due to spatial persistence of particle velocities on a characteristic length scale (see also section 3.2). High temporal correlation of low velocities is reflected in the peak at 0 of $p_\Delta(\eta)$ in Figure 4, while correlation and variability of velocities is echoed in the heavy tails.

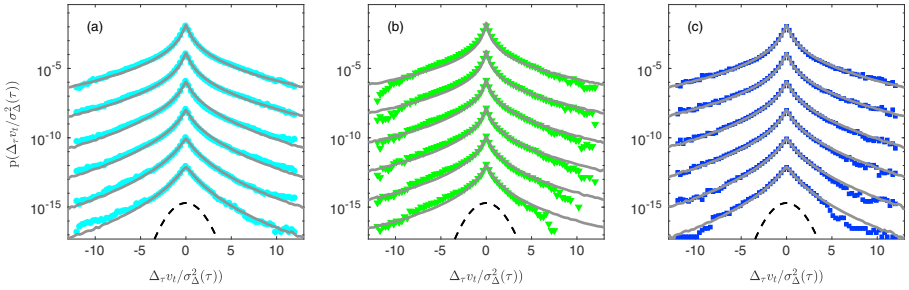

Figure 4. Probability distribution of velocity increments from normalized t-Lagrangian velocities (symbols) and their respective CTRW model simulations (gray lines) for samples (a) *A*, (b) *B*, and (c) *C*. Increments are determined at time lags of $\tau = 0.05\tau_v$, $0.1\tau_v$, $0.33\tau_v$, $0.5\tau_v$, τ_v, and $2\tau_v$, arranged from top to bottom. Dashed black line is a reference Gaussian distribution.

4. Stochastic Particle Motion

As pointed out in section 3.2, particle motion in steady flow fields is characterized by the correlation scale λ_v of particle velocities along trajectories. This property can explain the signatures of intermittency that are observed in the velocity time series in Figure 2, and the distributions of velocity increments in Figure 4. The persistence of particle velocities in space causes strong temporal correlation of slow particle motion and rapid variability of high velocities. These features can be quantified systematically by the continuous time random walk framework [*de Anna et al.*, 2013; *Holzner et al.*, 2015], which captures particle motion by a space time random walk. The particle motion is described by a characteristic transition length, the correlation scale λ_v, and a random transition time determined by the particle velocity $v_s(s)$. The velocity statistics are obtained by equidistant sampling of particle velocities along trajectories. The PDF $p_s(v)$ of the s-Lagrangian PDF is related to the t-Lagrangian velocity through flux weighting [*Dentz et al.*, 2016]. Thus, we set here the steady s-Lagrangian velocity PDF equal to the flux-weighted late time t-Lagrangian velocity PDF, $p_\ell(v)$

$$p_s(v) = \frac{v p_\ell(v)}{\langle v_\ell \rangle}. \tag{10}$$

We consider that under ergodic conditions, the late time t-Lagrangian velocity PDF is equal to the Eulerian velocity PDF. The evolution of the particle velocity PDF from early to late times, as discussed in section 3.3, can be quantified with the CTRW approach by modeling the series of s-Lagrangian velocities $v_s(s)$ as a Markov process in s [*Dentz et al.*, 2016]. In the following, we present a CTRW model based on a velocity Markov process that explains the evolution of the mean and centered mean square displacement and the distributions of velocity increments in terms of the pore-scale velocity distribution and its spatial organization.

4.1. Velocity Markov Process

We observe in section 3.3 that the bulk of the distributions of particle velocities can be modeled by a log-normal function. This implies that the distribution of the log-velocity $w_s(s) = \ln[v_s(s)]$ is Gaussian. Hence, to model the evolution of $w_s(s)$, we use the Ornstein-Uhlenbeck process [*Gardiner*, 2010], whose steady state distribution is given by a Gaussian. As pointed out in section 3.4, the Ornstein-Uhlenbeck process has been used in the literature to model the evolution of temporal particle velocity series. Here we use it to model the evolution of the s-Lagrangian velocity in distance s along streamlines. The evolution of $w_s(s)$ then is given by

$$\frac{\mathrm{d}w_s(s)}{\mathrm{d}s} = -\lambda_v^{-1}\left[w_s(s) - M_s\right] + \sqrt{\frac{2\Sigma_s^2}{\lambda_v}}\xi(s), \tag{11}$$

where $\xi(s)$ is a Gaussian white noise with zero mean and covariance $\langle \xi(s)\xi(s')\rangle = \delta(s-s')$. The covariance of $w_s(s)$ decays exponentially as $\exp(-s/\lambda_v)$ and thus reflects the correlation of $v_s(s)$ on the scale λ_v discussed in section 3.2. As given by equation (10) the corresponding steady state velocity PDF $p_s(v)$ is obtained from $p_\ell(v)$ through flux weighting. Thus, the mean M_s and variance Σ_s^2 are related to M_ℓ and Σ_ℓ^2 given by equation (8) as

$$M_s = M_\ell + \Sigma_\ell^2, \qquad \Sigma_s^2 = \Sigma_\ell^2. \tag{12}$$

The PDF $p_w(w, s=0)$ is Gaussian as well and corresponds to the early time lognormal velocity PDF $p_e(v)$ such that its mean and variance are equal to M_0 and Σ_0^2 given by equation (8). The particle time, equation (3), at a given distance s along the trajectory is given by

$$\frac{\mathrm{d}t(s)}{\mathrm{d}s} = \exp[-w_s(s)]. \tag{13}$$

The particle velocity $v_t(t)$ is given in terms of $w_s(s)$ as

$$v_t(t) = \exp\{w_s[s(t)]\}, \qquad s(t) = \sup[s|t(s) \le t]. \tag{14}$$

Mean and mean square displacements, as well as the PDF of velocity increments, are determined in the same way as the experimental data. It is interesting to note that the process for $w_t(t) = w_s[s(t)] = \ln[v_t(t)]$ is given by

$$\frac{\mathrm{d}w_t(t)}{\mathrm{d}t} = -\lambda_v^{-1}\left[w_t(t) - M_s\right]\exp[w_t(t)] + \sqrt{\frac{2\Sigma_s^2\exp[w_t(t)]}{\lambda_v}}\xi(t). \tag{15}$$

This means that the time evolution of the lognormal velocity process is characterized by a multiplicative noise as expressed by the exponential dependence on the right side of equation (15). A similar observation has been made in the analysis of numerical pore-scale velocity data [*Meyer and Bijeljic*, 2016].

The current approach differs from the previous model proposed by the authors [*Holzner et al.*, 2015] in the scale of the velocity evolution process simulated. The older model simulates the longitudinal velocity component on a coarse scale by use of a persistence term that allows a particle to maintain its velocity with a given probability. Such resolution cannot capture subpore fluctuations, as is reflected in the overestimation of the ballistic displacement behavior and inadequate distribution of particle accelerations. In contrast, the new model simulates the fluctuations of velocity magnitude on a fine scale by a white noise. This produces highly resolved subpore fluctuations and vastly improves model performance for displacements and acceleration distributions. In the following, we report on the numerical implementation of the velocity model (11) and its application to the experimental data.

4.2. Simulations and Application to Data

The numerical simulations are based on a simple Euler scheme for equation (11), which gives

$$w_{n+1} = w_n - \frac{\Delta s}{\lambda_v}(w_n - M_s) + \sqrt{\frac{2\Sigma_s^2 \Delta s}{\lambda_v}}\eta_n \tag{16}$$

where we set $w_n = w_s(s_n)$ with $s_n = n\Delta s$. η_n is a Gaussian random variable characterized by 0 mean and unit variance. The particle time is given by

$$t_{n+1} = t_n + \Delta s \exp(-w_n). \tag{17}$$

The particle velocity is now given by

$$v_t(t) = \exp(w_{n_t}), \qquad n_t = \sup(n|t_n \le t). \tag{18}$$

The particle displacement is given by $s(t) = s_{n_t}$. We use a discretization of $\Delta s = 10^{-5}$ m. Note that the scheme (16) is characterized by a constant velocity on the scale Δs. Thus, to properly quantify the velocity increment statistics it is necessary to choose a $\Delta s \ll \lambda_v$.

Figures 1a–1c show the experimental data and the simulation results based on equation (16) for the mean displacement. The velocity Markov model captures the early time evolution of $m(t)$ as well as the transition to the late time behavior. We observe a similar performance of the centered mean square displacement in Figures 1d–1f. Both the ballistic short time behavior as well as the transition to sub-ballistic are well represented by the space Markovian velocity model (11). Accurate representation of preasymptotic behavior sanctions long-term simulations to identify the time to reach a Fickian regime. We find this transition to occur at $t = 28\tau_v, 71\tau_v$, and $54\tau_v$ for structures *A*, *B*, and *C*, respectively (refer to the supporting information for more details).

A qualitative comparison between measured and simulated velocity series in Figure 2 shows that the model reproduces the intermittent characteristics remarkably well in terms of frequency, duration, and magnitude of high-velocity bursts. The collective performance of all simulated path lines is reflected in the global velocity distributions of Figure S7. The initial, late time, and global velocity distributions are captured by the Markov model. More critically, the distributions of Lagrangian velocity increments are in excellent agreement with the experimental distributions, see Figures 4 and S8, capturing even subtle differences in the tails of $p_\Delta(\eta;\tau)$ between the three structures.

The model is lastly evaluated for sensitivity to variations of the input values by carrying out bootstrap sampling of the trajectories. We randomly sample 1/3 of the recorded trajectories and use those data to compute new velocity PDFs and correlation lengths to run the model with. The process is repeated 50 times for each experiment. Figures J1, J3 and J5 illustrate the sensitivity of the model with variability of the input parameters (see distributions in Figures J2, J4 and J6). The small spread in the results demonstrates the robustness of the model even when considering input parameter uncertainty.

5. Conclusions

In summary, we have collected three-dimensional information of Lagrangian velocity experimentally using a novel imaging technique for heterogeneous porous media samples. A velocity magnitude process is proposed

and implemented in a correlated CTRW model that uses the spatial discretization of Lagrangian velocities. We show that our simple model can be directly parameterized from velocity distributions to capture transport behavior and intermittent dynamics. In particular, the model faithfully reproduces the preasymptotic mean and mean squared displacement in the ballistic and superdiffusive regimes. The model is also able to quantify the nonstationarity of velocity statistics. We expect that our approach can be used in a variety of applications in nature where flow behaviors are inherently nonstationary and intermittent over a range of scales leading to anomalous transport behaviors and incomplete mixing.

Acknowledgments
V.L.M. acknowledges the financial support of the AXA Research Fund. M.D. gratefully acknowledges the support of the European Research Council (ERC) through the project MHetScale (grant agreement 617511) and the support of the Spanish Ministry of Economy, Industry and Competitivity through the project MECMAT (CGL2016-80022-R). M.H. acknowledges the financial support of the Swiss National Foundation (grants 44645 and 172916). Raw particle tracking data are available with the supporting information.

References

Armstrong, R. T., and D. Wildenschild (2012), Investigating the pore-scale mechanisms of microbial enhanced oil recovery, *J. Pet. Sci. Eng.*, *94–95*, 155–164.
Berkowitz, B., A. Cortis, M. Dentz, and H. Scher (2006), Modeling non-Fickian transport in geological formations as a continuous time random walk, *Rev. Geophys.*, *44*, RG2003, doi:10.1029/2005RG000178.
Bijeljic, B., A. H. Muggeridge, and M. J. Blunt (2004), Pore-scale modeling of longitudinal dispersion, *Water Resour. Res.*, *40*, W11501.
Bijeljic, B., A. Q. Raeini, P. Mostaghimi, and M. J. Blunt (2013), Predictions of non-Fickian solute transport in different classes of porous media using direct simulation on pore-scale images, *Phys. Rev. E*, *87*(1), 13011.
Blunt, M. J. (2001), Flow in porous media–pre-network models and multiphase flow, *Curr. Opinion Colloid Interf. Sci.*, *6*(3), 197–207.
Blunt, M. J., B. Bijeljic, H. Dong, O. Gharbi, S. Iglauer, P. Mostaghimi, A. Paluszny, and C. Pentland (2013), Pore-scale imaging and modelling, *Adv. Water Res.*, *51*, 197–216.
Bolster, D., M. Dentz, and T. Le Borgne (2009), Solute dispersion in channels with periodically varying apertures, *Phys. Fluids*, *21.5*, 56601.
Clotet, X., J. Ortín, and S. Santucci (2014), Disorder-induced capillary bursts control intermittency in slow imbibition, *Phys. Rev. Lett.*, *113*(7), 74501.
Datta, S. S., H. Chiang, T. S. Ramakrishnan, and D. A. Weitz (2013), Spatial fluctuations of fluid velocities in flow through a three-dimensional porous medium, *Phys. Rev. Lett.*, *111*(6), 64501.
de Anna, P., T. Le Borgne, M. Dentz, A. M. Tartakovsky, D. Bolster, and P. Davy (2013), Flow intermittency, dispersion, and correlated continuous time random walks in porous media, *Phys. Rev. Lett.*, *110*(18), 184502.
de Anna, P., J. Jimenez-Martinez, H. Tabuteau, R. Turuban, T. Le Borgne, M. Derrien, and Y. Meheust (2014), Mixing and reaction kinetics in porous media: An experimental pore scale quantification, *Environ. Sci. Technol.*, *48*(1), 508–516.
Dentz, M., and B. Berkowitz (2003), Transport behavior of a passive solute in continuous time random walks and multirate mass transfer, *Water Resour. Res.*, *39*(5), WR001163.
Dentz, M., T. Le Borgne, A. Englert, and B. Bijeljic (2011), Mixing, spreading and reaction in heterogeneous media: A brief review, *J. Contam. Hydrol.*, *120*, 1–17.
Dentz, M., P. K. Kang, A. Comolli, T. Le Borgne, and D. R. Lester (2016), Continuous time random walks for the evolution of Lagrangian velocities, *Phys. Rev. Fluids*, *1*, 74004.
Dong, H., and M. J. Blunt (2009), Pore-network extraction from micro-computerized-tomography images, *Phys. Rev. E*, *80*(3), 36307.
Fatt, I. (1956), *The network model of porous media: I. Capillary pressure characteristics*, 144–159, vol. 207.
Freedman, D. L., and J. M. Gossett (1989), Biological reductive dechlorination of tetrachloroethylene and trichloroethylene to ethylene under methanogenic conditions, *Appl. Environ. Microb.*, *55*, 2144–2151.
Gardiner, C. (2010), *Stochastic Methods*, Springer Verlag, Berlin-Heidelberg.
Helton, J. C. (1993), Uncertainty and sensitivity analysis techniques for use in performance assessment for radioactive waste disposal, *Reliability Eng. Syst. Safety*, *42*, 327–367.
Hiorth, A., L. M. Cathles, and M. V. Madland (2010), The impact of pore water chemistry on carbonate surface charge and oil wettability, *Transp. Porous Med.*, *85*(1), 1–21.
Holzner, M., M. Willmann, V. L. Morales, and M. Dentz (2015), Intermittent Lagrangian velocities and accelerations in three-dimensional porous medium flow, *Phys. Rev. E*, *92*, 13015.
Hoyer, K., M. Holzner, B. LÃijthi, M. Guala, A. Liberzon, and W. Kinzelbach (2005), 3D scanning particle tracking velocimetry, *Exp. Fluids*, *39*(5), 923–934.
Kang, P. K., P. de Anna, J. P. Nunes, B. Bijeljic, M. J. Blunt, and R. Juanes (2014), Pore-scale intermittent velocity structure underpinning anomalous transport through 3-D porous media., *Geophys. Res. Lett.*, *41*, 6184–6190, doi:10.1002/2014GL061475.
Kang, P. K., M. Dentz, T. Le Borgne, and R. Juanes (2015), Anomalous transport on regular fracture networks: Impact of conductivity heterogeneity and mixing at fracture intersections, *Phys. Rev. E*, *92*(2), 22148.
Koch, D. L., and J. F. Brady (1985), Dispersion in fixed beds, *J. Fluid Mech.*, *154*, 399–427.
Le Borgne, T., M. Dentz, and J. Carrera (2008), Lagrangian statistical model for transport in highly heterogeneous velocity fields, *Phys. Rev. Lett.*, *101*(9), 90601.
Le Borgne, T., D. Bolster, M. Dentz, P. de Anna, and A. Tartakovsky (2011), Effective pore-scale dispersion upscaling with a correlated continuous time random walk approach, *Water Resour. Res.*, *47*, W12538.
Lester, D. R., G. Metcalfe, and M. G. Trefry (2014), Anomalous transport and chaotic advection in homogeneous porous media, *Phys. Rev. E*, *90*(6), 63012.
McCarthy, G. J., W. B. White, and D. E. Pfoertsch (1978), Synthesis of nuclear waste monazites, ideal actinide hosts for geologic disposal, *Mat. Res. Bull.*, *13*, 1239–1245.
Meyer, D. W., and B. Bijeljic (2016), Pore-scale dispersion: Bridging the gap between microscopic pore structure and the emerging macroscopic transport behavior, *Phys. Rev. E*, *94*, 13107.
Neuman, S. P. (1990), Universal scaling of hydraulic conductivities and dispersivities in geologic media, *Water Resour. Res.*, *26*(8), 1749–1758.
Pope, S. B. (2000), *Turbulent Flows*, Cambridge Univ. Press, Cambridge, UK.
Siena, M., M. Riva, J. D. Hyman, C. L. Winter, and A. Guadagnini (2014), Relationship between pore size and velocity probability distributions in stochastically generated porous media, *Phys. Rev. E*, *89*(1), 13018.
Sund, N., D. Bolster, and C. Dawson (2015), Upscaling transport of a reacting solute through a peridocially converging–diverging channel at pre-asymptotic times, *J. Contaminant Hydr.*, *182*, 1–15.
Tyukhova, A., M. Dentz, W. Kinzelbach, and M. Willmann (2016), Mechanisms of anomalous dispersion in flow through heterogeneous porous media, *Phys. Rev. Fluids*, *1*, 74002.

Willmann, M., J. Carrera, X. Sanchez-Vila, O. Silva, and M. Dentz (2010), Coupling of mass transfer and reactive transport for nonlinear reactions in heterogeneous media, *Water Resour. Res.*, *46*(7), W07512.
Xu, H. (2008), Tracking Lagrangian trajectories in position-velocity space, *Meas. Sci. Technol.*, *19*(7), 75105.
Zhang, W.-x. (2003), Nanoscale iron particles for environmental remediation: An overview, *J. Nanopart. Res.*, *5*, 323–332.